Computational and Structural Biotechnology Journal 21 (2023) 2640–2653

Contents lists available at ScienceDirect

Computational and Structural Biotechnology Journal

journal homepage: www.elsevier.com/locate/csbj

Research Article

The impact of pathogenic and artificial mutations on Claudin-5 selectivity from molecular dynamics simulations

Alessandro Berselli [a,b,1], Giulio Alberini [a,c,1], Fabio Benfenati [a,c,*], Luca Maragliano [a,d,*]

[a] Center for Synaptic Neuroscience and Technology (NSYN@UniGe), Istituto Italiano di Tecnologia, Largo Rosanna Benzi, 10, 16132 Genova, Italy
[b] Department of Experimental Medicine, Università degli Studi di Genova, Viale Benedetto XV, 3, 16132, Genova, Italy
[c] IRCCS Ospedale Policlinico San Martino, Largo Rosanna Benzi, 10, 16132, Genova, Italy
[d] Department of Life and Environmental Sciences, Polytechnic University of Marche, Via Brecce Bianche, 60131, Ancona, Italy

ARTICLE INFO

Article history:
Received 15 February 2023
Received in revised form 3 April 2023
Accepted 3 April 2023
Available online 12 April 2023

Keywords:
BBB paracellular proteins
Paracellular permeability
Tight junctions
Claudin-based paracellular models
Protein complexes
Structural modeling
Molecular dynamics

ABSTRACT

Tight-junctions (TJs) are multi-protein complexes between adjacent endothelial or epithelial cells. In the blood-brain-barrier (BBB), they seal the paracellular space and the Claudin-5 (Cldn5) protein forms their backbone. Despite the fundamental role in brain homeostasis, little is known on Cldn5-based TJ assemblies. Different structural models were suggested, with Cldn5 protomers generating paracellular pores that restrict the passage of ions and small molecules. Recently, the first Cldn5 pathogenic mutation, G60R, was identified and shown to induce Cl^--selective channels and Na^+ barriers in BBB TJs, providing an excellent opportunity to validate the structural models. Here, we used molecular dynamics to study the permeation of ions and water through two distinct G60R-Cldn5 paracellular architectures. Only the so-called Pore I reproduces the functional modification observed in experiments, displaying a free energy (FE) minimum for Cl^- and a barrier for Na^+ consistent with anionic selectivity. We also studied the artificial Q57D and Q63D mutations in the constriction region, Q57 being conserved in Cldns except for cation permeable homologs. In both cases, we obtain FE profiles consistent with facilitated passage of cations. Our calculations provide the first in-silico description of a Cldn5 pathogenic mutation, further assessing the TJ Pore I model and yielding new insight on BBB's paracellular selectivity.

1. Introduction

The blood-brain barrier (BBB) is a highly selective interface that separates the capillary blood flow from the brain parenchyma, and it is composed of brain endothelium, pericytes and astrocytes. Brain endothlial cells are tightly bound at their lateral membranes by multimeric protein complexes named tight junctions (TJs) [1–3] that are minimally permeable to solutes. TJ proteins are organized in continuous networks of transmembrane strands, and are responsible for strictly regulating the diffusion of solutes through the intercellular space between cells, named the paracellular space. Understanding their molecular mechanisms and dysfunctions has a very high clinical potential [4,5].

Claudin 5 (Cldn5) is the most abundant component of the BBB TJ strands and serves as their backbone. The Cldn5 topology is characterized by a bundle of four transmembrane helices (TM1–4) with two extracellular loops (ECL1–2), cytoplasmic N- and C-terminal residues, and an intracellular loop [2]. To generate TJs, Cldn5 proteins assemble via *cis*- (intracellular) interactions within each endothelial cell membrane and *trans*- (intercellular) interactions across adjacent cells. The physiological function of Cldn5 as a regulator of paracellular transport makes it a relevant target in the development of novel strategies to deliver drugs directly to the brain. However, structure-based approaches are still limited by our incomplete understanding of how Cldn5 generates high-order complexes.

Recently, different structural models were proposed as building blocks of Cldn5 paracellular architectures [6–8]. Two of them [6,7], usually called Pore I and Pore II models, give rise to a pore cavity in the paracellular space, and their validity was investigated also for other Cldns, homologous to Cldn5, and expressed in non-neural

* Corresponding authors at: Center for Synaptic Neuroscience and Technology (NSYN@UniGe), Istituto Italiano di Tecnologia, Largo Rosanna Benzi, 10, 16132 Genova, Italy.
E-mail addresses: fabio.benfenati@iit.it (F. Benfenati), l.maragliano@univpm.it (L. Maragliano).
[1] These authors contributed equally to this work

https://doi.org/10.1016/j.csbj.2023.04.001

Nomenclature

BBB	blood-brain barrier.
CLDN	claudin.
CV	collective variable.
ECL	extracellular loop.
FF	force field.
FE	free energy.
MD	molecular dynamics.
POPC	1-palmitoyl-2-oleoyl-sn-glycero-3-phosphocholine.
TJ	tight junction.
TM	trans-membrane.
US	umbrella sampling.
WHAM	weighted histogram analysis method.

tissues [9–12–15–18–21,22]. While Pore I was first proposed for Cldn15 based on experimental observations [10], Pore II was originally suggested by computational studies [7]. Albeit different, both configurations are formed by two *cis* dimers that associate paracellularly to generate a tetramer encompassing a pore. Remarkably, in the case of Cldn5, molecular dynamics (MD) simulations showed that both pores do not allow the permeation of ions or small molecules through the paracellular space, in line with Cldn5's known barrier function [23,24]. In our previous work [24], we calculated the free energy (FE) profiles of single ions/water molecules translocating across the two Cldn5 models, revealing that both structures oppose to ionic permeation, but are permissive to water.

The first *de novo* Cldn5 mutation linked to a neurological disorder was recently reported [25]. The variation, G60R, is located in the ECL1 domain and is associated with two unrelated cases of alternating hemiplegia with microcephaly. Experiments showed that, while the mutation does not alter the formation of TJs by Cldn5, it strongly affects its barrier function, by inducing high permeability for Cl^- and low permeability for Na^+. The discovery and the characterization of this mutation provides an excellent opportunity to further assess the two aforementioned structural models of Cldn5 complexes. Here, we performed umbrella sampling (US) MD simulations to calculate the FE for permeation of single Na^+, Cl^- and H_2O molecules through the two models for $Cldn5^{G60R}$, and compared the results with those of $Cldn5^{WT}$ [24]. Notably, only Pore I, where the arginine side chain is located near the central constriction site, reproduces the experimentally observed change in ion selectivity induced by the mutation. Indeed, the mutated Pore I Cl^- and Na^+ FE profiles along the channel axis are characterized by an attractive minimum and a repulsive barrier, respectively, thus suggesting the formation of an anionic channel.

With these results at hand, and to further test the validity of the Pore I model, we performed the same calculations after the mutation of two glutamine residues, also located at the central constriction site of the Cldn5 structure, into aspartate (Q57D and Q63D, respectively). Q57 is conserved among various Cldns, with some relevant exceptions including Cldn15 and Cldn10b, where the glutamine is replaced by an aspartate that plays a pivotal role in conferring ionic selectivity to the paracellular channels [12,15]. As expected, we observed that both mutations modify the FE profile, making it attractive to cations and repulsive to anions.

This study provides an *in-silico,* atom-level rationale, explaining the effect of a pathogenic mutation on the Cldn5-mediated BBB paracellular properties. Altogether, our findings further validate the Pore I model for the paracellular arrangement of Cldn5, revealing it as the sole consistent with all the available experimental observations. By identifying the protein-protein surface at the core of TJ Cldn5 assemblies, our computational investigation provides a step forward in the establishment of a robust basis for rational design of small molecules capable of modulating the BBB paracellular permeability in a safe and reversible manner.

2. Materials and methods

2.1. The configurations of the single Cldn5 pores and MD parameters

In order to perform the simulations for the mutated Cldn5 systems, we started from two equilibrated wild type (WT) configurations of the single pore models (Pore I and Pore II), described in our previous work [24]. In addition to the insertion of the mutations, we added counterions in both solvent exposed regions, in order to neutralize the system. Briefly, each model includes four Cldn5 protomers (two for each *cis*- configuration), two membrane bilayers formed by 1-palmitoyl-2-oleoyl-SN-glycero-3-phosphocholine (POPC) molecules, water molecules and ions. The G60R mutation was included in each Cldn5 subunit with the help of UCSF Chimera [26], and the initial configurations of the arginine side chains were selected from the Dunbrack rotamers library [27]. The resulting systems were refined with GalaxyRefineComplex [28,29], embedded in a double POPC bilayer, solvated with explicit water molecules and neutralized with counterions. CHARMM hydrogen atoms were added with CHARMM-GUI [30–32] and disulfide bonds were assigned to the couples of conserved cysteine residues, according to the information provided in the Cldn15 structure identified by the PDB ID: 4P79. The $Cldn5^{Q57D}$ and $Cldn5^{Q63D}$ Pore I systems were generated in the same way.

As in our previous works [11,24], we used the NAMD software [33]. All the simulations were performed in the *NPT* ensemble (P = 1 atm, T = 310 K), employing the Nosé-Hoover Langevin piston method [34,35] and a Langevin thermostat. Following the details of the CHARMM-GUI configuration files for NAMD, the oscillation

Table 1
Summary of the MD simulations performed in this work (G60R, Q57D, Q63D systems). We also report the achieved cumulative time for the WT systems, already shown in our previous work [24].

Model	System	Permeating ion	Time (ns)
Pore I	G60R	Na^+	10 × 60 = 600
Pore I	G60R	Cl^-	40 × 60 = 2400
Pore I	G60R	H_2O	10 × 60 = 600
Pore II	G60R	Na^+	10 × 65 = 650
Pore II	G60R	Cl^-	30 × 65 = 1950
Pore II	G60R	H_2O	10 × 65 = 650
Pore I	Q57D	Na^+	20 × 60 = 1200
Pore I	Q57D	Cl^-	10 × 60 = 600
Pore I	Q57D	H_2O	10 × 60 = 600
Pore I	Q63D	Na^+	30 × 60 = 1800
Pore I	Q63D	Cl^-	20 × 60 = 1200
Pore I	Q63D	H_2O	10 × 60 = 600
Pore I	WT	Na^+	15 × 60 = 900
Pore I	WT	Cl^-	40 × 60 = 2400
Pore I	WT	H_2O	10 × 60 = 600
Pore II	WT	Na^+	20 × 65 = 1300
Pore II	WT	Cl^-	20 × 65 = 1300
Pore II	WT	H_2O	20 × 65 = 1300

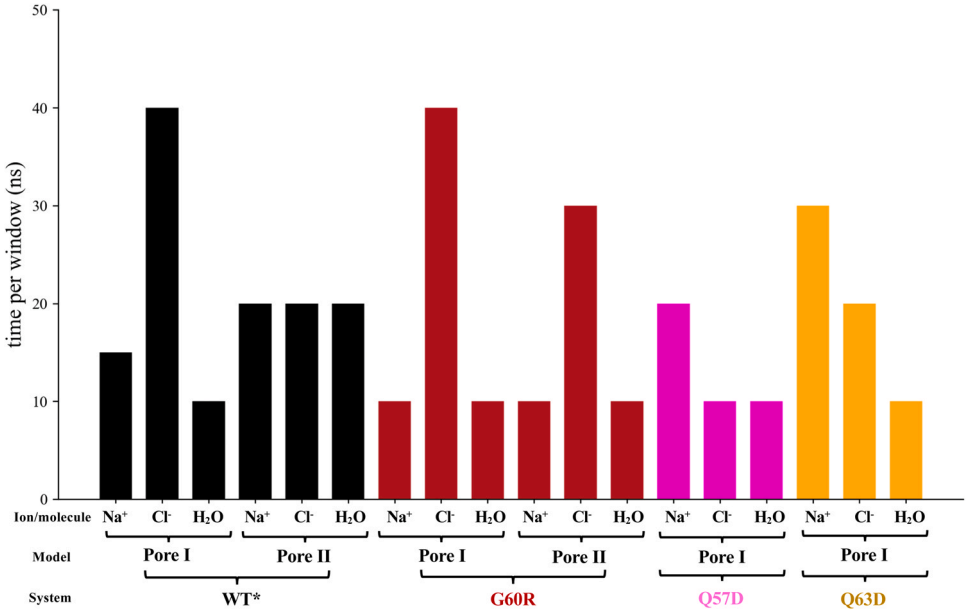

Fig. 1. Simulated time per window (in ns) for each US calculation of Cldn5 systems studied in this article (G60R, Q57D, Q63D) and in our previous work [24] (WT).

period of the piston was set at 50 fs, and the damping time scale at 25 fs. The damping coefficient of the Langevin thermostat was set at 1 ps^{-1}.

The CHARMM36m [36–38]/CHARMM36[39] parameters were used for the protein and lipids, respectively, together with the TIP3P model for water molecules [40] and the associated ionic parameters with NBFIX corrections [41–43]. Electrostatic and van der Waals interactions were calculated with a cutoff of 12 Å as prescribed by the CHARMM force field. A switching function was applied starting to take effect at 10 Å to obtain a smooth decay. Hexagonal periodic boundary conditions were adopted to limit the size of the system. Long range electrostatic interactions were calculated using the Particle Mesh Ewald (PME) algorithm [44], adopting a spline interpolation order 6. A maximum space between grid points of 1.0 Å was used, as implemented in CHARMM-GUI. All covalent bonds involving hydrogen atoms were constrained using the SHAKE/SETTLE algorithms [45,46], in order to use a time-step of 2 fs. To ensure maximum accuracy, electrostatic and van der Waals interactions were computed at each simulation step [24].

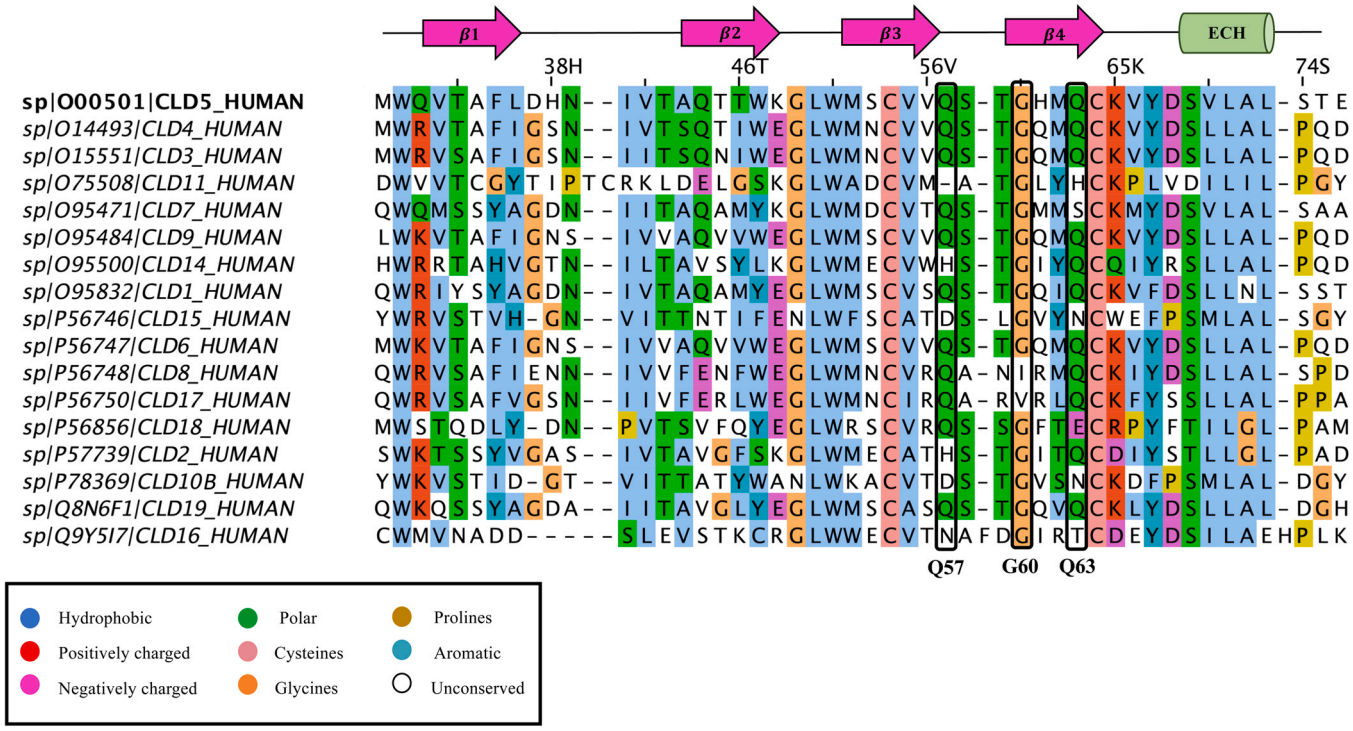

Fig. 2. Multiple sequence alignment of hCldn5 and other hCldn proteins (ECL1 region only). This analysis includes classic Cldns (1–10, 14, 15, 17, 19) and two non-classic Cldns (11, 18). Each sequence is identified by the following entry: sp / UNIPROT (https://www.uniprot.org) ID / Cldn name. Colours are assigned according to the legend included in the picture. The numbering above the sequences is related to the Cldn5 protein. Secondary structure elements associated with the ECL1 topology are shown above the sequences as arrows (β1 to β4 strands) or cylinders (ECH α-helix). The Cldn5 residues corresponding to the mutations studied in this article (Q57, G60, Q63) are indicated by black rectangles.

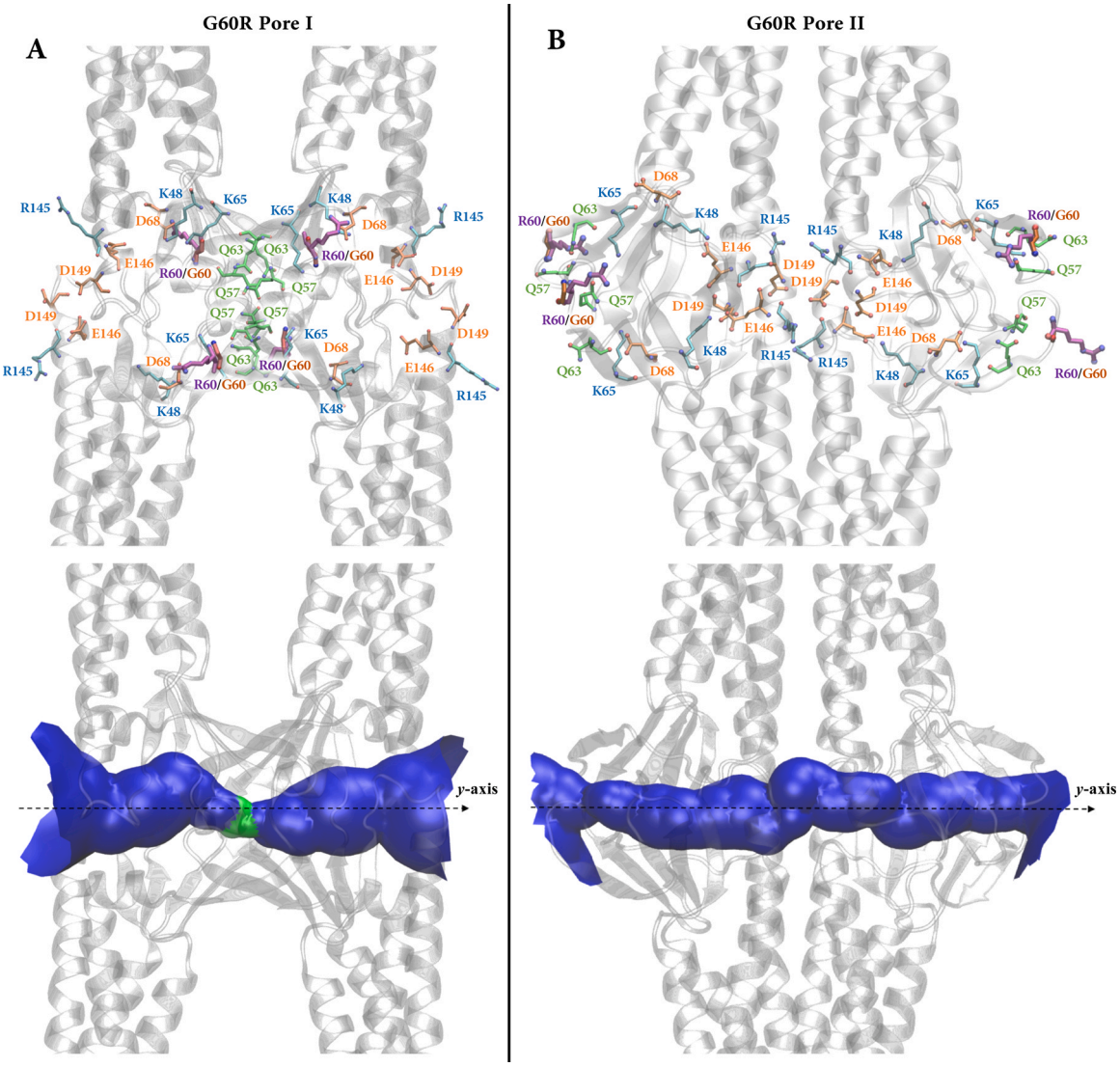

Fig. 3. Equilibrated structures of Cldn5^{G60R} Pore I (A) and Pore II (B). The four protomers are represented as gray ribbons. The side chains of the pore lining residues are represented as sticks (upper row) and the mutated G60R side chains are colored in purple. In the lower row, the pore cavity is shown as a surface, calculated by the HOLE program. The green color indicates the region where the pore size is that of one water molecule. The dashed line (*y* axis) represents the axis used in the US simulations for ion/water permeation.

Consistent with the protocol of Ref. [24], an initial minimization and an additional 30-ns-long equilibration with progressive release of positional restraints were performed to achieve a stable starting configuration for US runs.

1D-US simulations with harmonic biases were performed with the Collective Variables (Colvar) module [47], using the projection of the ion position onto the axis of the paracellular channel as single collective variable (CV). The Weighted Histogram Analysis Method (WHAM) was used to reconstruct the 1D-FE, using the code from the Grossfield group, available at http://membrane.urmc.rochester.edu/content/wham. During US simulations, we employed harmonic restraints for the C_α atoms of the same set of residues for each paracellular model introduced in Ref. [24] to avoid orientational and translational displacements that could affect the FE calculations.

2.2. Umbrella sampling simulations for the single Cldn5 pores

We performed 1D-FE calculations of ion/water permeation through the paracellular cavities, following the same protocol used in our previous works [12,13,24]. In umbrella sampling (US) calculations [48], a harmonic potential energy term is added to the CHARMM terms of the MD potential to ensure efficient sampling along the chosen CV in different independent simulations (named *windows*). In the case of our 1D CV, indicated as *y*, these potentials are expressed as:

$$\hat{\omega}_i(y) = \frac{1}{2}\hat{\kappa}(y - y_i^0)^2 \tag{1}$$

where y_i^0 indicates the value at which the CV is restrained in window i and $\hat{\kappa}$ is a constant. For an appropriate choice of $\hat{\kappa}$, a sufficient overlap between the sampled distributions of adjacent windows is obtained and the final, full FE calculations can be obtained by employing WHAM [49,50].

We performed US simulations with the harmonic restraints of Eq. (1) and $\hat{\kappa} = 2$ kcal/(mol · Å^2). We employed a total of at least 60 windows with a uniform spacing of 1 Å. The time length required for convergence for each window is shown in Table 1 and in Fig. 1. For each window, the frames from the first ns were removed and not used for analysis. To optimize the use of parallel computational resources, we prepared a number of starting conformations where the tested ion or the H_2O oxygen atom was swapped with equilibrated water molecules, for the whole length of the paracellular axis. Ions

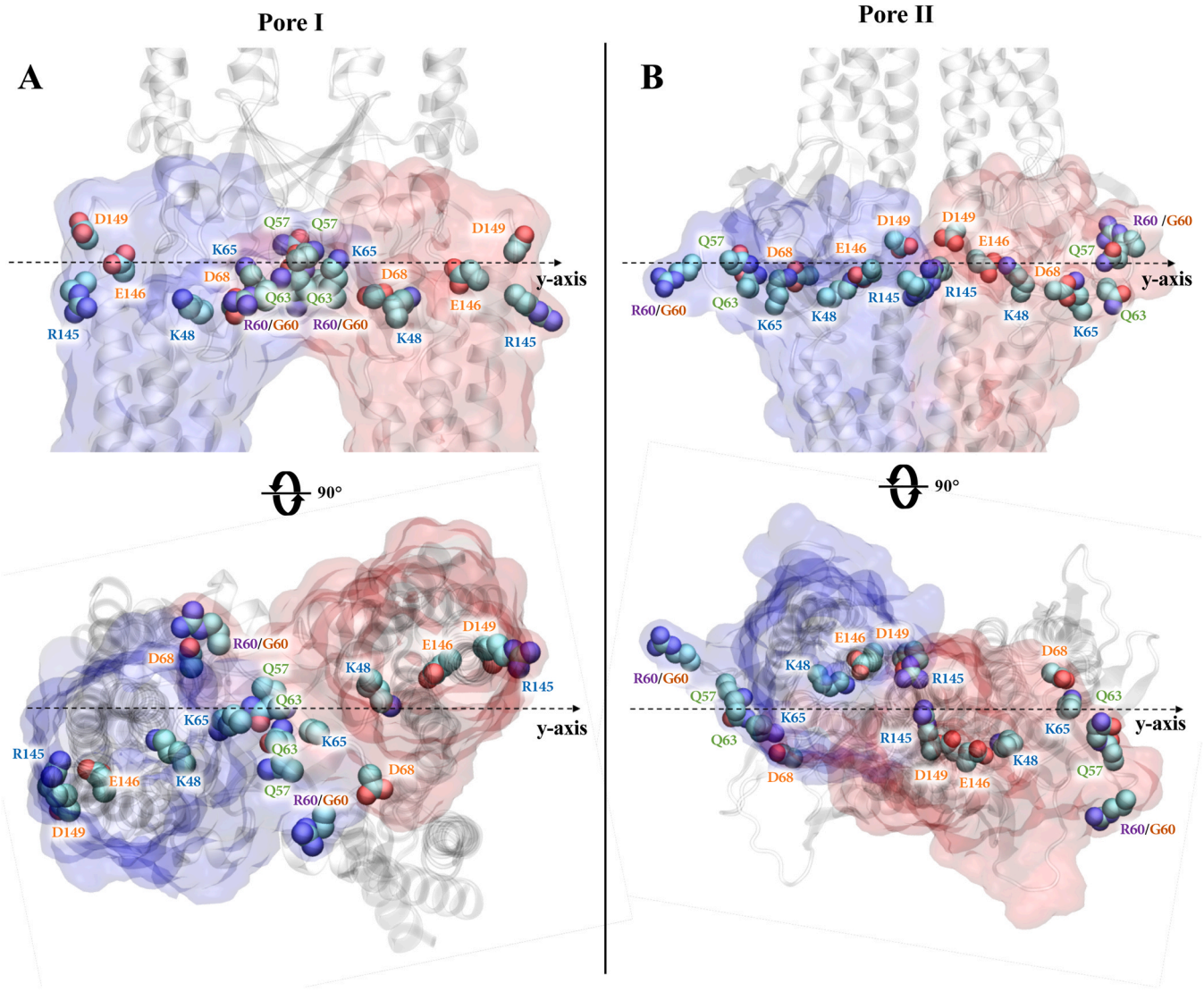

Fig. 4. Pore axis and cavity lining amino acids in the Cldn5^{G60R} Pore I (**A**) and Pore II (**B**) models. The upper row shows an enlarged lateral view, with surface representation of two *cis*-interacting protomers (blue and red) and residues as spheres. The lower row shows a cut-away view of the pores, with only two subunits in blue and red surfaces. The dashed line (*y* axis) represents the axis used in the FE calculation for ion/water permeation.

not involved in the CV definition were excluded from the paracellular cavity by applying two half-harmonic potentials, one for each entrance, characterized by an elastic constant of 10 kcal/(mol · Å^2).

In addition, the displacement of the ion orthogonal to the pore axis is confined within a disk of radius $r_0 + \delta$, where r_0 is the pore radius as determined by the HOLE program [51,52] and $\delta = 2$ Å, by means of a force constant of 2 kcal/mol [24].

For WHAM analysis, we used 600 bins, and a tolerance of 0.0001. Furthermore, we used bootstrapping to evaluate the statistical uncertainty at each bin, using 100 bootstrap trials [12]. Overall, the US calculations are based on a cumulative production of 12.8 μs.

2.3. Pore dimensions of the paracellular cavities in the Pore I models

The pore radius profile was calculated with the HOLE program [51,52]. The analysis was performed for the structures resulting from the MD simulations carried out in each window of the US protocol used for the FE calculation of water permeation. In addition, the pore radius calculations was also performed for the structures resulting from MD simulations of windows 1–5 and 55–60 of Na^+ and Cl^- US protocol. In these windows, the labeled ion is still in the solvent and it does not affect the dimension of the pore cavity. A total of 80 snapshots were analyzed, and the result is reported as the average pore radius profile ± standard deviation.

2.4. Multi-Pore I models

Three additional triple-pore assemblies were constructed based on Pore I, one using Cldn5^{WT} and two using Cldn5^{G60R} protomers. Each structure includes 16 Cldn5 subunits. We modeled the human Cldn5 (hCldn5^{WT}) monomer by homology, using SWISS-MODEL [53] and the crystallographic Cldn15 structure (PDB ID: 4P79 [9]) as template. The Cldn5^{WT} triple-pore model was built using as reference the extended, multi-pore configuration proposed by Suzuki et al. in Ref. [10] for the homologous Cldn15. The G60R mutation was included in Cldn5 subunits with the help of UCSF Chimera [26]. The two Cldn5^{G60R} multimer models, named Triple-Pore1-version A (TP1A) and Triple-Pore1-version B (TP1B), differ in the orientation of the R60 side chains in each pore. In TP1A, these are oriented outside the pore formed by their protomers, toward the lumens of adjacent pores, while in TP1B they are inside their respective protomers' pore. The three multimeric systems were refined with GalaxyRefineComplex [28,29], embedded in a double POPC bilayer and

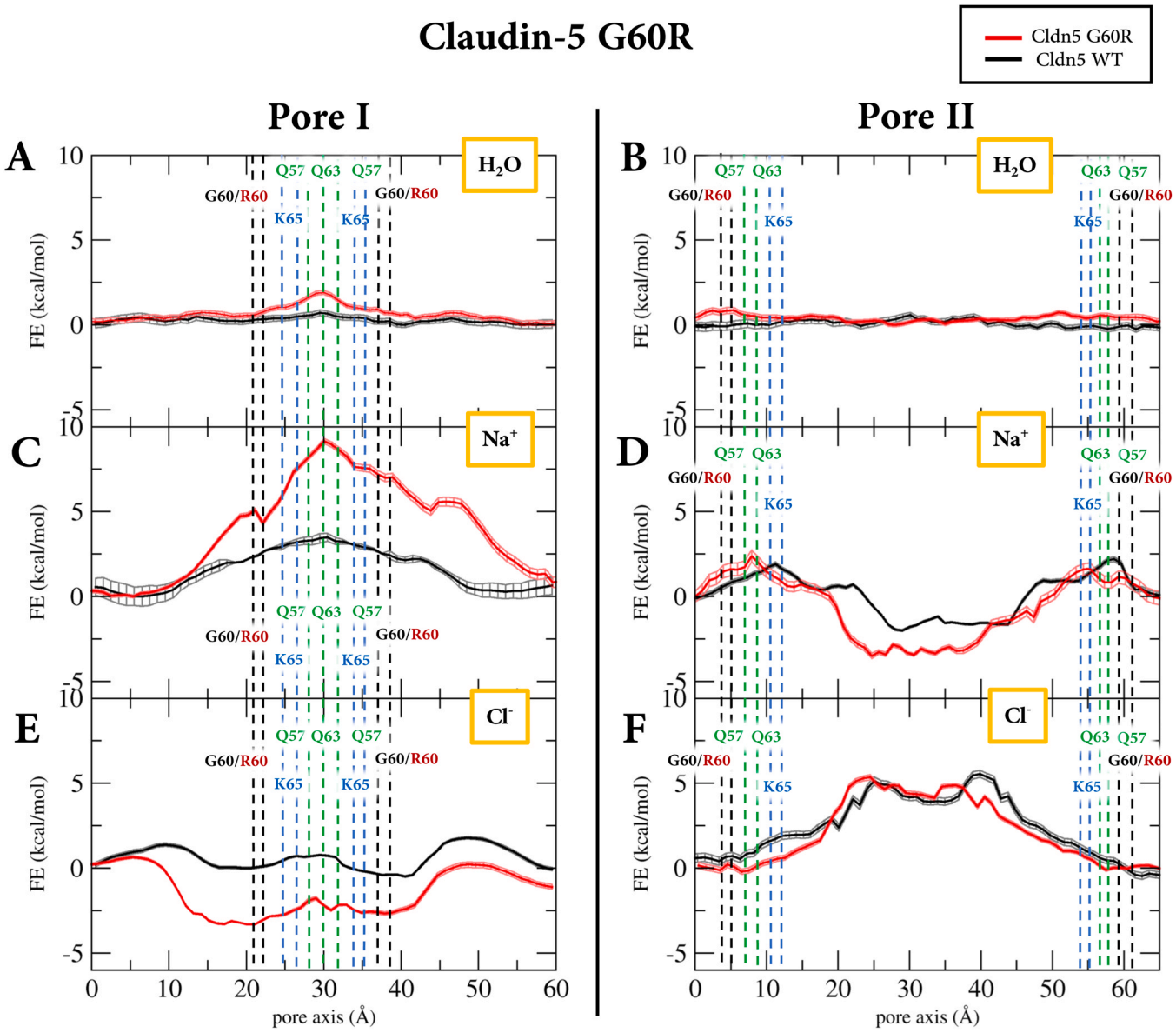

Fig. 5. FE profiles for H_2O, Na^+ and Cl^- translocation across the pore axis of both Pore I (**A**, **C**, **E**) and Pore II (**B**, **D**, **F**) systems. Red and black lines represent values for the G60R mutant and the WT, respectively. The positions of the C_α atoms of Q57, G60R, Q63 and K65 are reported as dashed lines.
(WT data reproduced with permission from Ref. [24], Copyright 2022, licensed under CC BY).

solvated with water molecules. Energy minimization was performed, followed by 100 ns of equilibration with progressive release of positional restraints.

2.5. Electrostatic potential maps

We calculated the electrostatic potential maps for the single- and triple-pore structures based on Pore I, for $Cldn5^{WT}$ and $Cldn5^{G60R}$. Calculations were performed with the adaptive Poisson-Boltzmann solver code [54], using the default parameters set by the developers.

2.6. Structural analysis

All the MD trajectories were visualized and analyzed using UCSF Chimera [26] (www.cgl.ucsf.edu/chimera/), the NAMD-COLVAR module [47] and VMD [55] (www.ks.uiuc.edu/Research/vmd/) with Tcl scripts.

2.7. Alignment of sequences

The alignment of multiple Cldn sequences was performed using the Clustal Omega program [56,57] available in Jalview [58].

3. Results

3.1. The pathogenic and artificial mutations involve highly conserved residues in the Cldn family

As in all other Cldns, the ECL1 and ECL2 domains of human Cldn5 (hCldn5) are organized in a β-sheet formed by five antiparallel strands, named β1 to β5. The first four strands belong to ECL1 and the fifth one to ECL2. The ECL1 domain is stabilized by a conserved disulfide bond formed by two cysteine residues belonging to β3 and β4. An additional extracellular helix (named ECH) is observed between β4 and the second transmembrane helix (TM2). In Fig. 2, we show a multi-sequence alignment of a selection of human Cldn proteins. Interestingly, G60 is located in a region where mutations

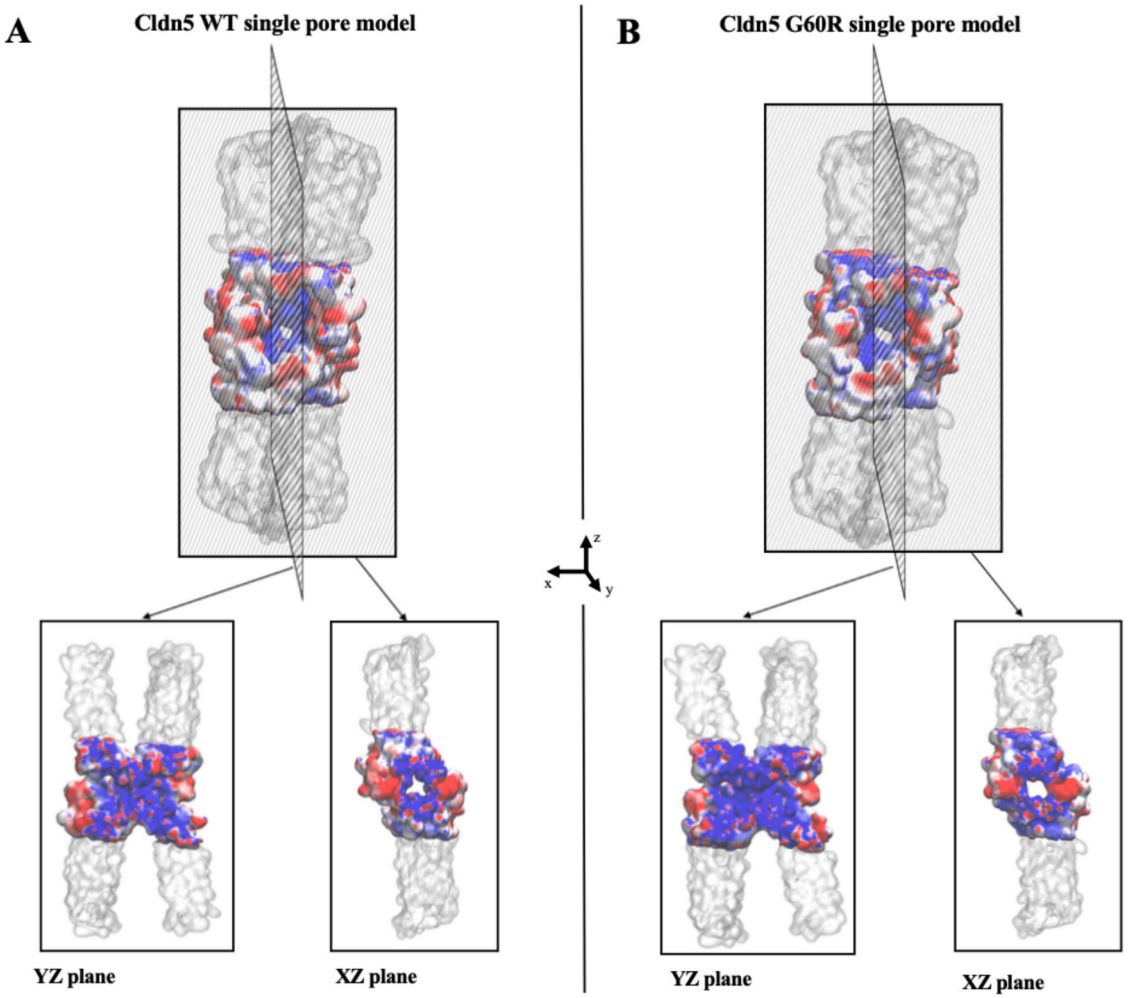

Fig. 6. Electrostatic potential maps as molecular surfaces of Cldn5^{WT}(**A**) and Cldn5^{G60R} (**B**) Pore I models. Upper row: apical view (*xz* plane); lower row: cross-section of the lateral view (*yz* plane, left) and cut-away view from the apical side (*xz* plane, right), with only two Cldn5 subunits. Energy values are represented with a color-code ranging from red (− 5 kT/e) to white to blue (+5 kT/e).

are predicted to be deleterious [25], and is conserved among all the sequences with two exceptions: Cldn17, which is known to form paracellular channels with distinct anionic selectivity [59], and Cldn8, which is essential for the TJ localization of Cldn-4 in the kidney [60].

The other two mutants (Q57D and Q63D) affect residues located in the same portion of the ECL1 domain, between β3 and β4 (Q57), and on β4 (Q63). In the cation-selective, channel-forming, Cldn15 and Cldn10b proteins, an aspartate is found at the position equivalent to Cldn5 Q57[2], which prompted us to investigate the effect of the Q57D variant in the Cldn5 pore model.

3.2. The G60R mutation induces an anion-selective channel in Pore I but not in Pore II

In order to perform the FE calculations of ion/water translocation through the mutated paracellular structures, we inserted the G60R variant in the WT configurations of both pore models. The equilibrated structures of Cldn5^{G60R} Pore I and II are shown in Fig. 3. Due to the different orientation of the monomers, the mutated residues are located near the center of the cavity in Pore I and at the end-points of the cavity in Pore II (Fig. 4). In Pore I, while the side chains of Q57, Q63 and K65 point toward the interior of the pore, the G60R side chains are oriented toward the exterior; conversely, in Pore II, the side chains of Q57, Q63 and K65 are located at the mouths of the pore, and the G60R side chains are exposed to the solvent. Hence, in both structures the four mutated side chains point outside the pore vestibule.

The FE profiles for the G60R Cldn5 structures are reported in Fig. 5, and compared with analogous profiles for the WT Cldn5 pores as calculated by us in Ref.[24] (data reproduced with permission). Results show that the two models remain permeable to water after the insertion of the mutation, which induces only a small FE barrier in proximity of the mutated residues in Pore I (Fig. 5A,B). Water translocation across the BBB is known to be characterized by limited exchange rate [61–63] and, to the best of our knowledge, there is no evidence to rule out water exchange through the Cldn5 paracellular pathways. Indeed, all computational investigations of the WT Cldn5 pores performed so far revealed water permeable cavities. [7,23,24].

On the other hand, Na^+ translocation is affected in the Cldn5^{G60R} Pore I (Fig. 5C), where the four added arginine side chains cause an increase of the central FE peak from 2.5-3 kcal/mol to 8.5–9 kcal/mol. In Pore II, the difference between the WT and the Cldn5^{G60R} Na^+ FE profiles lies mainly at the center of the pore, where the mutations deepen the energy minimum by about 1–2 kcal/mol, while the barriers at the pore's end-points are essentially preserved (Fig. 5D), in line with the location of the substituted arginine side chains. In the case of Cl^-, the mutated Pore I displays a minimum deeper than the WT of approximately − 2.5 kcal/mol for 10 Å $\leq z \leq$ 45 Å (Fig. 5E), consistent with the location of the arginines and with the function of

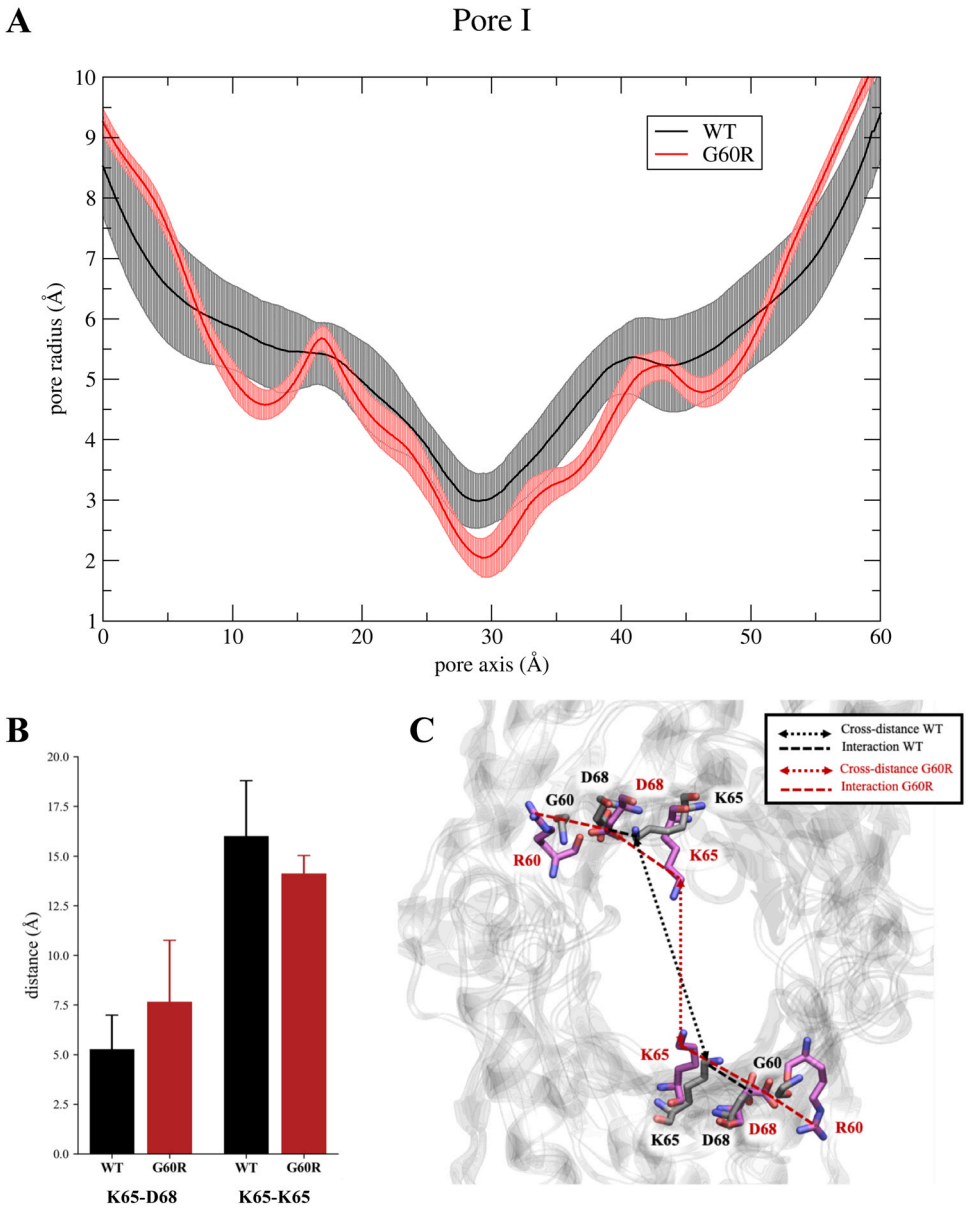

Fig. 7. (**A**) Average pore radius (with standard deviation) calculated along the pore axis for the WT and G60R Pore I. (**B**) Average cross-distances of selected pore-lining residues. (**C**) Snapshots from simulations of WT and mutated system showing different pore-lining residues conformations.

an anionic channel. Conversely, the FE profile of Cl^- translocation in the G60R Pore II is essentially the same as in the WT configuration (i.e., a repulsive barrier; Fig. 5F), as a consequence of the different position of the mutated residues along the main axis of the paracellular cavity.

3.3. The G60R mutation changes the electrostatic field and the geometry of the Cldn5 Pore I structure

Electrostatic potential maps for the $Cldn5^{WT}$and $Cldn5^{G60R}$ Pore I models are shown as molecular surfaces in Fig. 6. The comparison reveals an increase of positively charged regions (colored in blue) within the mutated pore, consistent with the minimum of the FE for Cl^- translocation shown for the mutated Pore I.

A comparison between the size of the pore in WT and mutated structures is shown in Fig. 7. Despite the change in electrostatics, the four R60 side chains cause a reduction of the pore radius at the central constriction region (Fig. 7A). The average cross-distances between residues lining the pores, calculated along the MD trajectories of the same US windows used for pore radius, reveal the origin of this change: in the mutated pore, the R60 side chains interact with the adjacent D68 residues, perturbing its interaction with K65 that is observed in the WT pore, and letting the K65 side chains free to relocate toward the solvated lumen of the pore (Fig. 7B and **C**).

3.4. The Q57D and Q63D mutations convert Pore I into a cationic paracellular channel

To further investigate the effect of pore-lining mutations in Pore I, we calculated the water/ion translocation FE profiles for the artificial mutants Q57D and Q63D. The locations of these residues are reported in Fig. 8. The glutamine in position 57 is highly conserved among Cldn proteins, with the notable exception of Cldn15 (D55) and Cldn10b (D56), which are known to be cation permeable [2,64]. Results published in Ref.s [11,12,15,65,66] assessed the validity of the Pore I model for these members of the Cldn family, suggesting that they attract cations through the paracellular space thanks to the

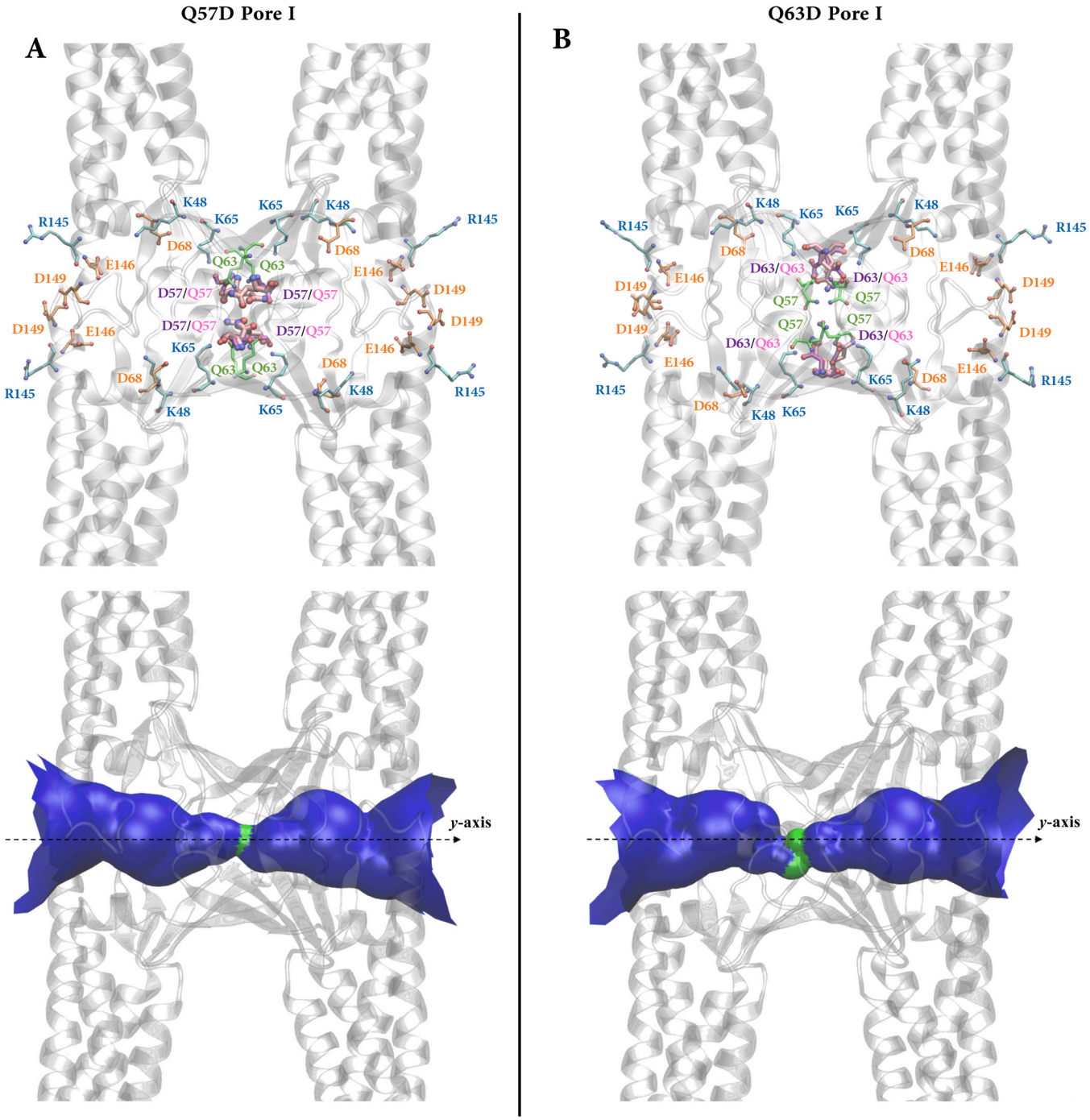

Fig. 8. Representative pictures of Pore I Cldn5^{Q57D} (**A**) and Cldn5^{Q63D} (**B**) structures. The four Cldn5 proteins are represented as gray ribbons. The pore lining residues are reported (upper row), with their side chains represented as sticks. The mutated Q57D and Q63D side chains are colored in purple. In the lower row, the pore cavity is shown as a surface, calculated by the HOLE program. The green color indicates the region where the pore size is that of one water molecule. The dashed line (*y* axis) represents the axis used in the US FE simulations for ion/water permeation.

formation of a tetra-aspartate cage formed by the D55/D56 side chains at the pore constriction. Q63 is also highly conserved in Cldns, but it is substituted by an asparagine in Cldn15 and Cldn10b. Based on these observations, we asked ourselves whether point mutations resulting in the insertion of negative charges in this critical region could transform the impermeable Cldn5^{WT} pore to an artificial paracellular cation channel. We thus generated Cldn5^{Q57D} and Cldn5^{Q63D} mutants and studied the effect of the mutations on water and ion translocation.

Our results based on US simulations of single Na^+, Cl^- and H_2O through the Cldn5^{Q57D} and Cldn5^{Q63D} Pore I configurations are shown in Fig. 9, and compared again with the WT system. Both mutations allow the structure to remain permissive to water paracellular diffusion (Fig. 9A,B). As for Na^+ translocation, they abolish the FE barrier in the central constriction seen in the WT system and cause the formation of a minimum. While the FE minimum of the Q63D mutation is localized in a narrow region of the paracellular space (at 25 Å $\leq z \leq$ 30 Å) and is modestly deep ($\sim$ 2 kcal/mol, Fig. 9D), the Q57D substitution induces a broader (20 Å $\leq z \leq$ 40 Å) and deeper minimum ($\sim$ 5 kcal/mol, Fig. 9C), confirming the paramount role of this residue in the regulation of the paracellular traffic. Finally, both mutations also modify the FE of Cl^- translocation,

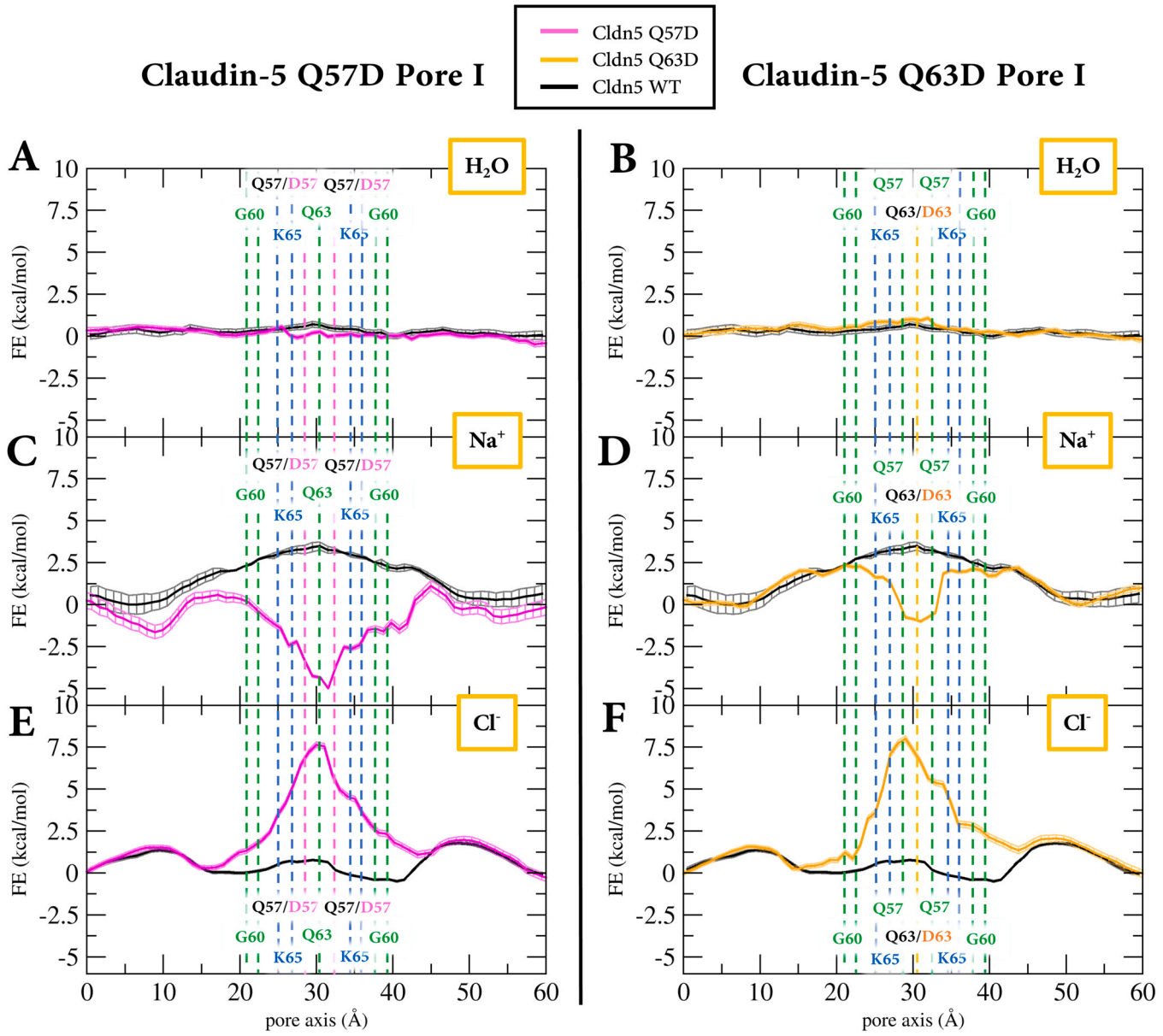

Fig. 9. FE profiles for H_2O, Na^+ and Cl^- translocation across the pore axis of the Q57D (**A**, **C**, **E**) and Q63D (**B**, **D**, **F**) Pore I systems. Black lines indicate profiles calculated for the WT systems. The positions of the C_α atoms of Q57(D), G60, Q63(D) and K65 are reported as dashed lines.
(WT data reproduced with permission from Ref. [24], Copyright 2022, licensed under CC BY).

causing the appearance of a central FE peak at ~ 7.5 kcal/mol (Fig. 9E,F). Remarkably, the results for Na^+ and Cl^- in the Q57D Pore I are consistent with our previous calculations for Cldn15 in the same configuration [12].

4. Discussion

Cldn5 is an essential protein for maintaining the BBB microenvironment, thus representing a novel target in the development of molecules to permeate the barrier in a safe and reversible manner. In lack of detailed experimental information, several structural models of Cldn5 tight junctional assemblies have been proposed, and their investigation, refinement and validation are mandatory steps to unravel the molecular basis of its function. To this goal, the recent discovery of the first Cldn5 variant associated with a neurological condition (G60R) [25] serves as an excellent bench test. The substitution, causing alternating hemiplegia in two unrelated patients, affects an amino acid of a loop between the β3 and β4 strands on ECL1, and was experimentally demonstrated to promote anion permeability in Cldn5 TJs. When inserted into two of the most studied models of Cldn5 single-pore structures, the mutation produced markedly different effects, allowing us to identify the one model displaying the experimentally observed anion-channel property. This is the so-called Pore I system, derived originally from the architecture of Cldn15 TJs proposed by Suzuki et al. [10], and first introduced for Cldn5 by Irudayanathan et al. [6] In this model, G60 is located close to the middle of the pore cavity and its substitution with an arginine strongly affects ion permeation, generating an attractive energy minimum for chloride and a repulsive barrier for sodium. Detailed analysis revealed that the mutation causes changes in both the electrostatic and structural properties of the pore, by inducing a broader positively charged molecular surface and a restriction of the cavity at the central region.

Additional simulations showed that other mutations (Q57D and Q63D, also at the center of the pore) have the effect of converting the Cldn5 complex into a cation channel. Q57 corresponds to D55 and

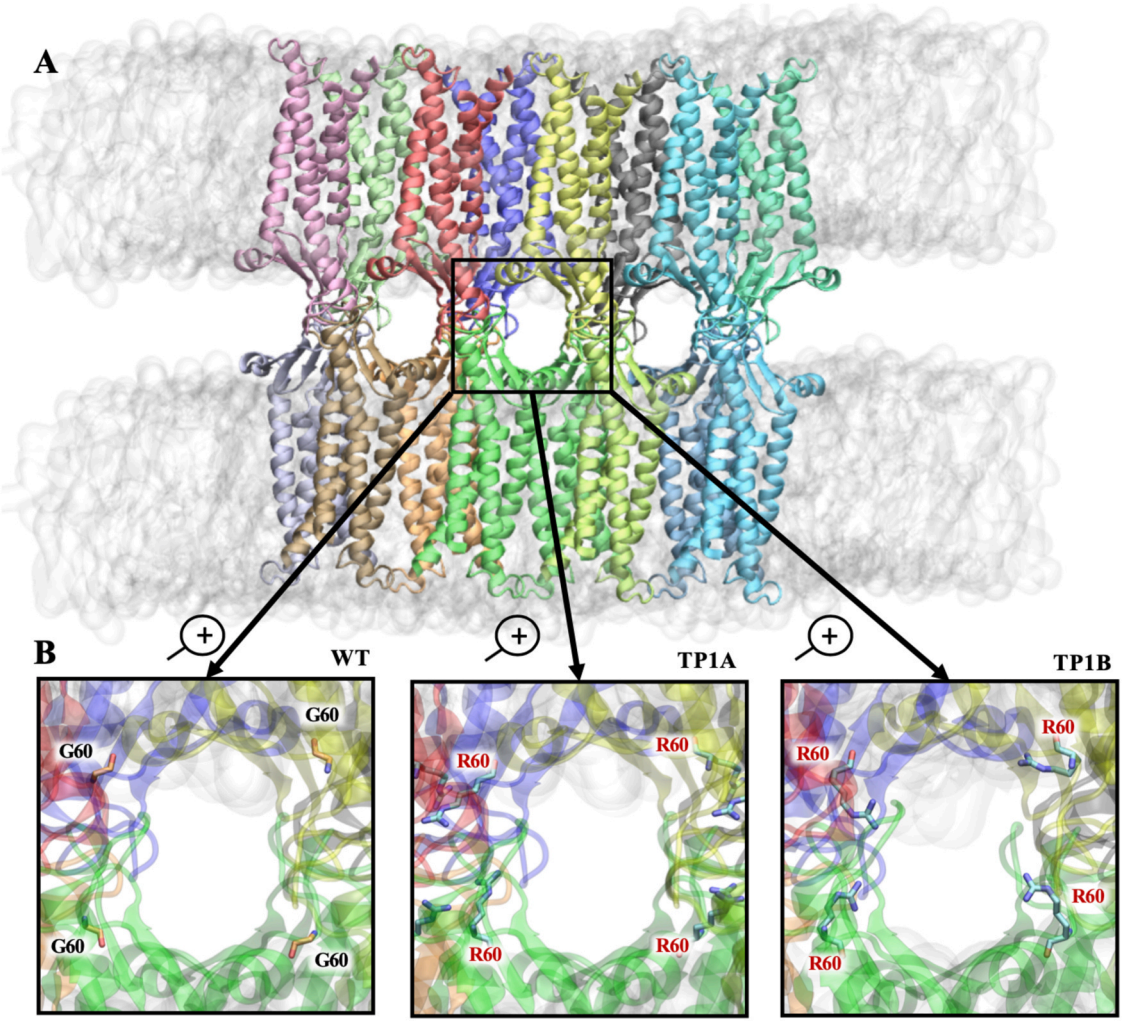

Fig. 10. **(A)** Modeling of triple pores, based on multiple Pore-I like structures. The proteins (ribbon style) are embedded in a double POPC bilayer. **(B)** Apical view of the central cavity for Cldn5^{WT} (left) and Cldn5^{G60R} (TP1A and TP1B, center and right, respectively). Details of modeling are described in the text.

D56 in the cation selective Cldn15 and Cldn10b, for which the validity of Pore I, and the specific role of the aspartic acid, have been assessed [11,12,15,65,66]. Since in Ref. [67] a decrease of *trans*-interactions was observed for Cldn5^{Q57D} in HEK-293 cells and no information is available to link these mutations to pathogenic variants of Cldn5, the main objective of our calculations was to determine whether the designed mutant architecture would have a channel function similar to that of the Cldns for which Pore I is a validated structure.

The study of ion translocation through Cldn-based paracellular cavities is a quite recent and promising research field in the context of MD simulations.

The results presented in this manuscript are based on the investigation of single and isolated tetrameric pores, not considering the role of the Cldn subunits in the TJ strand that are adjacent to the pore cavity. This strategy, already employed by us [12,13,24] and others [6,23], allows to considerably reduce the size of the studied systems, while retaining the key molecular determinants of TJ selectivity. Indeed, our previous work on the Cldn15 single Pore I configuration [12] revealed the same selectivity properties of a multi-pore model [15]. However, the addition of neighboring protomers in the strand might improve the representation of the protein in the physiological environment, as various computational studies have suggested that Cldn polymerization can affect the paracellular structures [11,15,14,65,66,16,17]. For a preliminary assessment of the G60R mutation's impact on multi-pore Cldn5 systems, we prepared three additional assemblies comprising a triple pore made by adjacent Pore I units, one using Cldn5^{WT} and two using Cldn5^{G60R} protomers (Fig. 10). The latter two, named TP1A and TP1B, differ in the orientation of the R60 side chains: while in TP1A they point outside the pore formed by their protomers, as in our single-pore structure, in TP1B they are oriented toward the pore's lumen. We then calculated the electrostatic potential maps of the WT and the TP1B triple pores and reported them in Fig. 11. The comparison reveals a marked increase of positively charged regions (blue color) for the mutated system in the interior surface of each pore, consistent with what obtained for G60R single-pores (see Fig. 6), and with the features of an anion channel. Therefore, the G60R mutation is expected to enhance anion permeation also in extended, multi-pore structures.

It is also of relevance to point out that here and in our previous works [12] we calculated the FE profiles of single ions translocating across the pore. While it is very likely that multiple ions are involved in the conduction mechanism of paracellular channels, the single-ion FE is a central concept in permeation studies, since it determines

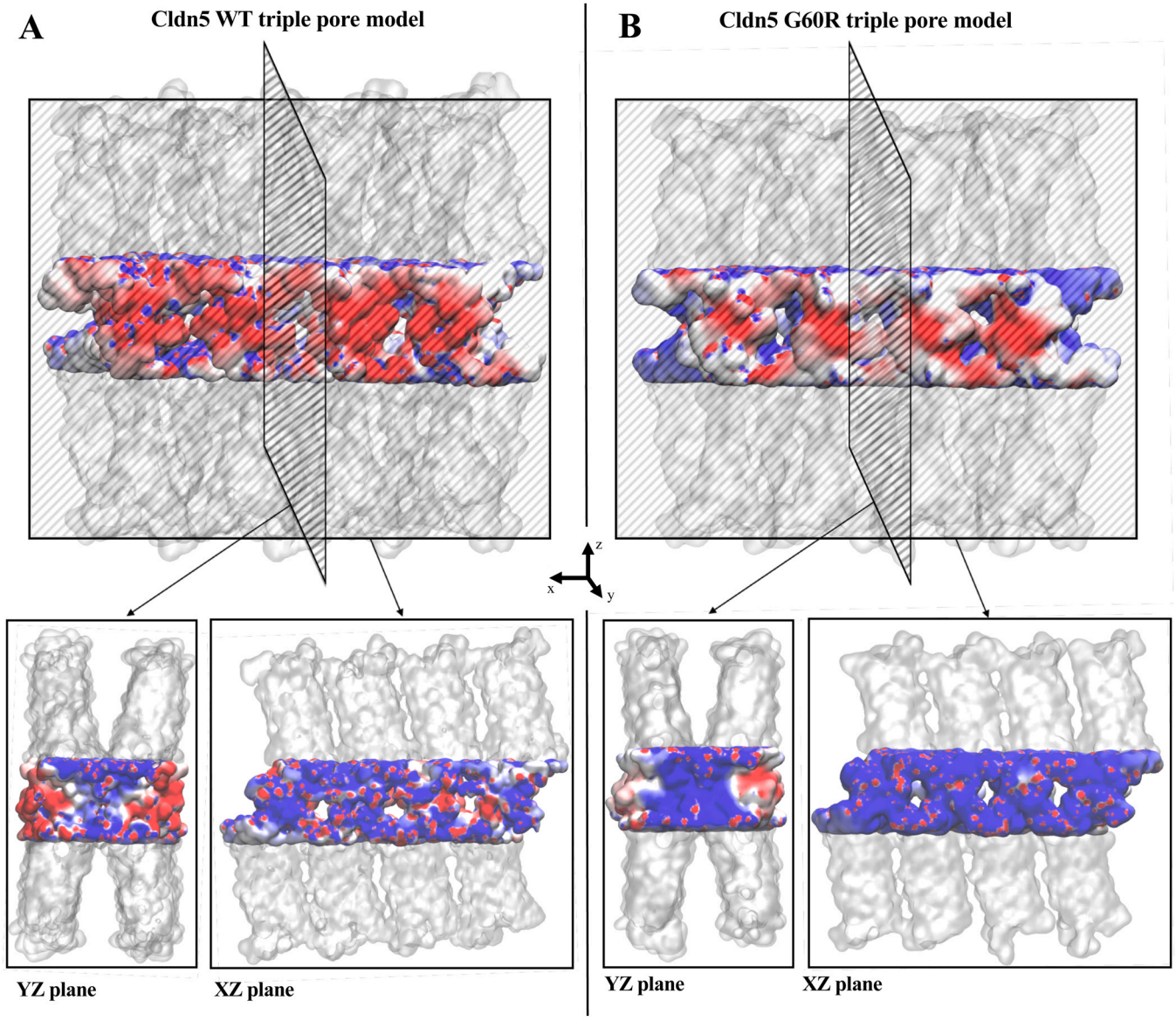

Fig. 11. Electrostatic potential maps as molecular surfaces for Cldn5^{WT}(**A**) and Cldn5^{G60R}, TP1B (**B**) Pore I models. Upper row: apical view (*xz* plane); lower row: cross-section of the lateral view (*yz* plane) and cut-away view from the apical side (*xz* plane). The color-code for energy values ranges from red (− 5 kT/e) to white to blue (+5 kT/e).

conduction at a relatively low ion concentration and yields fundamental information such as the location of binding sites and repulsive barriers, allowing for a preliminary screen of the effects of mutations or of distinct channel models.

The choice of the force field (FF) is another significant aspect of all-atom MD simulations that may have an impact on the results of ionic permeation through ion channels. In this study, we used the more recent version of the CHARMM FF (CHARMM36m [36–38]), in agreement with all available computational works on paracellular channels [6,7,11–14–17,18,23,24]. However, recent studies [68,69] revealed different outcomes from microsecond-long MD simulations of ion permeation through the selectivity filter of a voltage-gated potassium channel performed with CHARMM and another widely used FF, AMBER [70]. Hence, future investigations of Cldn-based pores will benefit from the integrated use of multiple FFs.

In conclusion, our results provide the first *in-silico* description of the effect of a Cldn5 pathogenic mutation. They agree in full with the recently reported experimental observations [25] and allow to discern the best pore model to describe the Cldn5 assembly in the BBB. By identifying protein-protein interfaces at the core of Cldn5 TJ assemblies, our computational investigation represents a step forward in the understanding of BBB structure and function, and in the structure-based search of opening agents for therapeutic treatments.

CRediT authorship contribution statement

Alessandro Berselli: Data curation, Formal analysis, Investigation, Visualization, Writing – review & editing. **Giulio Alberini**: Conceptualization, Formal analysis, Investigation, Project administration, Writing – original draft, Writing – review & editing. **Fabio Benfenati**: Funding acquisition and resources, Supervision, Writing – review & editing. **Luca Maragliano**: Conceptualization, Formal analysis, Funding acquisition and resources, Investigation, Project administration, Supervision, Writing – review & editing.

Declaration of Competing Interest

The authors declare that they have no known competing financial interests or personal relationships that could have appeared to influence the work reported in this paper.

Acknowledgments

We thank Mattia Pini and Sergio Decherchi for the kind assistance at Fondazione Istituto Italiano di Tecnologia computing center. We are grateful to Diego Moruzzo, Elisabetta Colombo and Andrea L. Benfenati for useful help. Computing time allocations were granted by the CINECA supercomputing center under the ISCRA initiative. We also gratefully acknowledge the HPC infrastructure at Fondazione Istituto Italiano di Tecnologia.

Funding

The research was supported by IRCCS Ospedale Policlinico San Martino (Ricerca Corrente and 5× 1000 grants to FB and LM), the Italian Ministry of Health (GR-2021-12372966 grant to FB) and by Telethon/Glut-1 Onlus Foundations (GSP19002_PAsGlut009 and GSA22A002 projects to FB).

Ethics statements

In this work, no potential identifiable human images or data are presented.

References

[1] Bonetta L. Endothelial tight junctions form the blood-brain barrier. J Cell Biol 2005;169:378.
[2] Günzel D, Yu ASL. Claudins and the modulation of tight junction permeability. Physiol Rev 2013;93:525.
[3] Berselli A, Benfenati F, Maragliano L, Alberini G. Multiscale modelling of claudin-based assemblies: a magnifying glass for novel structures of biological interfaces. Comput Struct Biotechnol J 2022;20:5984–6010.
[4] Hashimoto Y, Campbell M. Tight junction modulation at the blood-brain barrier: current and future perspectives. Biochim Biophys Acta Biomembr 2020;1862:183298.
[5] Luissint A-C, Artus C, Glacial F, Ganeshamoorthy K, Couraud P-O. Tight junctions at the blood brain barrier: Physiological architecture and disease-associated dysregulation. Fluids Barriers CNS 2012;9(23).
[6] Irudayanathan FJ, Trasatti JP, Karande P, Nangia S. Molecular architecture of the blood brain barrier tight junction proteins–a synergistic computational and in vitro approach. J Phys Chem B 2016;120:77.
[7] Irudayanathan FJ, Wang N, Wang X, Nangia S. Architecture of the paracellular channels formed by claudins of the blood-brain barrier tight junctions. Ann N Y Acad Sci 2017;1405:131.
[8] Rajagopal N, Nangia S. Unique structural features of claudin-5 and claudin-15 lead to functionally distinct tight junction strand architecture. Ann N Y Acad Sci 2022;1517(1):225–33.
[9] Suzuki H, Nishizawa T, Tani K, Yamazaki Y, Tamura A, Ishitani R, et al. Crystal structure of a claudin provides insight into the architecture of tight junctions. Science 2014;344:304.
[10] Suzuki H, Tani K, Tamura A, Tsukita S, Fujiyoshi Y. Model for the architecture of claudin-based paracellular ion channels through tight junctions. J Mol Biol 2015;427:291.
[11] Alberini G, Benfenati F, Maragliano L. A refined model of claudin-15 tight junction paracellular architecture by molecular dynamics simulations. PLoS ONE 2017;12:e0184190.
[12] Alberini G, Benfenati F, Maragliano L. Molecular dynamics simulations of ion selectivity in a claudin-15 paracellular channel. J Phys Chem B 2018;122:10783.
[13] Berselli A, Alberini G, Benfenati F, Maragliano L. Computational study of ion permeation through claudin-4 paracellular channels. Ann N Y Acad Sci 2022;1516(1):162–74.
[14] Zhao J, Krystofiak ES, Ballesteros A, Cui R, Van Itallie CM, Anderson JM, et al. Multiple claudin-claudin cis interfaces are required for tight junction strand formation and inherent flexibility. Commun Biol 2018;1:50.
[15] Samanta P, Wang Y, Fuladi S, Zou J, Li Y, Shen L, et al. Molecular determination of claudin-15 organization and channel selectivity. J Gen Physiol 2018;150(7):949–68.
[16] Fuladi S, McGuinness S, Khalili-Araghi F. Role of tm3 in claudin-15 strand flexibility: a molecular dynamics study. Front Mol Biosci 2022;9.
[17] Fuladi S, McGuinness S, Shen L, Weber CR, Khalili-Araghi F. Molecular mechanism of claudin-15 strand flexibility: a computational study. J Gen Physiol 2022;154(12). (11).
[18] Irudayanathan FJ, Wang X, Wang N, Willsey SR, Seddon IA, Nangia S. Self-assembly simulations of classic claudins-insights into the pore structure, selectivity, and higher order complexes. J Phys Chem B 2018;122:7463.
[19] Rajagopal N, Irudayanathan FJ, Nangia S. Palmitoylation of claudin-5 proteins influences their lipid domain affinity and tight junction assembly at the blood-brain barrier interface. J Phys Chem B 2019;123:983.
[20] Rajagopal N, Nangia S. Obtaining protein association energy landscape for integral membrane proteins. J Chem Theory Comput 2019;15:6444.
[21] Goliaei A, Adhikari U, Berkowitz ML. Opening of the blood-brain barrier tight junction due to shock wave induced bubble collapse: A molecular dynamics simulation study. ACS Chem Neurosci 2015;6(8):1296–301.
[22] Man VH, Li MS, Derreumaux P, Wang J, Nguyen TT, Nangia S, et al. Molecular mechanism of ultrasound interaction with a blood brain barrier model. J Chem Phys 2020;153(4):045104.
[23] Irudayanathan FJ, Nangia S. Paracellular gatekeeping: what does it take for an ion to pass through a tight junction pore? Langmuir 2020;36:6757.
[24] Berselli A, Alberini G, Benfenati F, Maragliano L. Computational assessment of different structural models for claudin-5 complexes in blood-brain barrier tight junctions. ACS Chem Neurosci 2022;13(14):2140–53.
[25] Hashimoto Y, Poirier K, Boddaert N, Hubert L, Aubart M, Kaminska A, et al. Recurrent de novo mutations in cldn5 induce an anion-selective blood-brain barrier and alternating hemiplegia. Brain 2022;145(10):3374–82.
[26] Pettersen EF, Goddard TD, Huang CC, Couch GS, Greenblatt DM, Meng EC, et al. Ucsf chimera — a visualization system for exploratory research and analysis. J Comput Chem 2004;25(13):1605–12.
[27] Shapovalov M, Dunbrack RJ. A smoothed backbone-dependent rotamer library for proteins derived from adaptive kernel density estimates and regressions. Structure 2011;19(6):844–58.
[28] Heo L, Lee H, Seok C. Galaxyrefinecomplex: refinement of protein-protein complex model structures driven by interface repacking. Sci Rep 2016;6:32153.
[29] Heo L, Park H, Seok C. Galaxyrefine: protein structure refinement driven by side-chain repacking. Nucleic Acids Res 2013;41:W384.
[30] Jo S, Lim JB, Klauda JB, Im W. Charmm-gui membrane builder for mixed bilayers and its application to yeast membranes. Biophys J 2009;97(1):50–8.
[31] Jo S, Kim T, Iyer V, Im W. Charmm-gui: a web-based graphical user interface for charmm. J Comput Chem 2008;29:1859–65.
[32] Jo S, Cheng X, Islam SM, Huang L, Rui H, Zhu A, et al. Charmm-gui pdb manipulator for advanced modeling and simulations of proteins containing non-standard residues. Adv Protein Chem Struct Biol 2014;96:235.
[33] Philips J, Braun R, Wang W, Gumbart J, Tajkhordshid E, Villa E, et al. Scalable molecular dynamics with namd. J Comput Chem 2005;26(16):1781–802.
[34] Feller SE, Zhang Y, Pastor RW, Brooks BR. Constant pressure molecular dynamics simulation: the langevin piston method. J Chem Phys 1995;103(11):4613–21.
[35] Martyna GJ, Tobias DJ, Klein ML. Constant pressure molecular dynamics algorithms. J Chem Phys 1994;101(5):4177–89.
[36] Huang J, Rauscher S, Nawrocki G, Ran T, Feig M, de Groot BL, et al. Charmm36m: an improved force field for folded and intrinsically disordered proteins. Nat Methods 2016;14:71–3.
[37] Best R, Zhu X, Shim J, Lopes P, Mittal J, Feig M, et al. Optimization of the additive charmm all-atom protein force field targeting improved sampling of the backbone phi, psi and side-chain chi(1) and chi(2) dihedral angles. J Chem Theory Comput 2012;8(09):3257–73.
[38] Huang J, MacKerell Jr AD. Charmm36 all-atom additive protein force field: validation based on comparison to nmr data. J Comput Chem 2013;34(25):2135–45.
[39] Klauda JB, Venable RM, Freites JA, O'Connor JW, Tobias DJ, Mondragon-Ramirez C, et al. Update of the charmm all-atom additive force field for lipids: validation on six lipid types. J Phys Chem B 2010;114(23):7830–43.
[40] Jorgensen W, Chandrasekhar J, Madura J, Impey R, Klein M. Comparison of simple potential functions for simulating liquid water. J Chem Phys 1983;79:926–35.
[41] Noskov S, Roux B. Control of ion selectivity in leut: two na^+ binding sites with two different mechanisms. J Mol Biol 2008;377(3):804–18.
[42] Luo Y, Roux B. Simulation of osmotic pressure in concentrated aqueous salt solutions. J Phys Chem Lett 2010;1(1):183–9.
[43] Venable RM, Luo Y, Gawrisch K, Roux B, Pastor RW. Simulations of anionic lipid membranes: development of interaction-specific ion parameters and validation using nmr data. J Phys Chem B 2013;117(35):10183–92.
[44] Darden T, York D, Pedersen L. Particle mesh ewald: an n ·log (n) method for ewald sums in large systems. J Chem Phys 1993;98(12):10089–92.
[45] Ryckaert J-P, Ciccotti G, Berendsen HJ. Numerical integration of the cartesian equations of motion of a system with constraints: molecular dynamics of n-alkanes. J Comput Phys 1977;23(3):327–41.
[46] Miyamoto S, Kollman PA. Settle: an analytical version of the shake and rattle algorithm for rigid water models. J Comput Chem 1992;13(8):952–62.
[47] Fiorin G, Klein ML, Hénin J. Using collective variables to drive molecular dynamics simulations. Mol Phys 2013;111(22–23):3345–62.
[48] Torrie GM, Valleau JP. Nonphysical sampling distributions in monte carlo free-energy estimation: umbrella sampling. J Comput Phys 1977;23:187.
[49] Souaille M, Roux B. Extension to the weighted histogram analysis method: combining umbrella sampling with free energy calculations. Comput Phys Commun 2001;135:40.
[50] Smith LG, Tan Z, Spasic A, Dutta D, Salas-Estrada LA, Grossfield A, et al. Chemically accurate relative folding stability of rna hairpins from molecular simulations. J Chem Theory Comput 2018;14:6598.
[51] Smart OS, Breed J, Smith GR, Sansom MS. A novel method for structure-based prediction of ion channel conductance properties. Biophys J 1997;72:1109.
[52] Smart OS, Neduvelil JG, Wang X, Wallace BA, Sansom MSP. Hole: a program for the analysis of the pore dimensions of ion channel structural models. J Mol Graph 1996;14:354.

[53] Waterhouse A, Rempfer C, Heer FT, Studer G, Tauriello G, Bordoli L, et al. Swiss-model: homology modelling of protein structures and complexes. Nucleic Acids Res 2018;46(W1):W296–303.
[54] Jurrus E, Engel D, Star K, Monson K, Brandi J, Felberg LE, et al. Improvements to the apbs biomolecular solvation software suite. Protein Sci 2018;27(1):112–28.
[55] Humphrey W, Dalke A, Schulten K. Vmd - visual molecular dynamics. J Mol Graph 1996;14(1):33–8.
[56] Goujon M, McWilliam H, Li W, Valentin F, Squizzato S, Paern J, et al. A new bioinformatics analysis tools framework at embl-ebi. Nucleic Acids Res 2010;38(suppl-2):W695–9.
[57] Sievers F, Wilm A, Dineen D, Gibson TJ, Karplus K, Li W, et al. Fast, scalable generation of high-quality protein multiple sequence alignments using clustal omega. Mol Syst Biol 2011;7(1):539.
[58] Waterhouse AM, Procter JB, Martin DMA, Clamp M, Barton GJ. Jalview version 2—a multiple sequence alignment editor and analysis workbench. Bioinformatics 2009;25(9):1189–91.
[59] Krug S, Günzel D, Conrad M, Rosenthal R, Fromm A, Amasheh S, et al. Claudin-17 forms tight junction channels with distinct anion selectivity. Cell Mol Life Sci: CMLS 2012;69:2765–78.
[60] Hou J, Renigunta A, Yang J, Waldegger S. Claudin-4 forms paracellular chloride channel in the kidney and requires claudin-8 for tight junction localization. Proc Natl Acad Sci USA 2010;107(42):18010–5.
[61] Shao X, Jann K, Ma S, Yan L, Montagne A, Ringman J, et al. Comparison between blood-brain barrier water exchange rate and permeability to gadolinium-based contrast agent in an elderly cohort. Front Neurosci e 2020;14:571480.
[62] Amasheh S, Schmidt T, Mahn M, Florian P, Mankertz J, Tavalali S, et al. Contribution of claudin-5 to barrier properties in tight junctions of epithelial cells. Cell Tissue Res 2005;321:89–96.
[63] Wen H, Watry DD, Marcondes MCG, Fox HS. Selective decrease in paracellular conductance of tight junctions: role of the first extracellular domain of claudin-5. Mol Cell Biol 2004;24(19):8408–17.
[64] Van Itallie CM, Rogan S, Yu A, Vidal LS, Holmes J, Anderson JM. Two splice variants of claudin-10 in the kidney create paracellular pores with different ion selectivities. Am J Physiol Ren Physiol 2006;291(6):F1288–99.
[65] Hempel C, Protze J, Altun E, Riebe B, Piontek A, Fromm A, et al. Assembly of tight junction strands: Claudin-10b and claudin-3 form homo-tetrameric building blocks that polymerise in a channel-independent manner. J Mol Biol 2020;432:2405.
[66] Hempel C, Rosenthal R, Fromm A, Krug SM, Fromm M, Günzel D, et al. Tight junction channels claudin-10b and claudin-15: functional mapping of pore-lining residues. Ann N Y Acad Sci 2022;1515(1):129–42.
[67] Piontek A, Rossa J, Protze J, Wolburg H, Hempel C, Günzel D, et al. Polar and charged extracellular residues conserved among barrier-forming claudins contribute to tight junction strand formation. Ann N Y Acad Sci 2017;1397(1):143–56.
[68] Furini S, Domene C. Critical assessment of common force fields for molecular dynamics simulations of potassium channels. J Chem Theory Comput 2020;16(11):7148–59.
[69] Ocello R, Furini S, Lugli F, Recanatini M, Domene C, Masetti M. Conduction and gating properties of the traak channel from molecular dynamics simulations with different force fields. J Chem Inf Model 2020;60(12):6532–43.
[70] Hornak V, Abel R, Okur A, Strockbine B, Roitberg A, Simmerling C. Comparison of multiple amber force fields and development of improved protein backbone parameters. Proteins 2006;65:712–25.